ACS APPLIED MATERIALS & INTERFACES

www.acsami.org Research Article

Protective Coating Interfaces for Perovskite Solar Cell Materials: A First-Principles Study

Azimatu Fangnon,* Marc Dvorak, Ville Havu, Milica Todorović, Jingrui Li, and Patrick Rinke

Cite This: *ACS Appl. Mater. Interfaces* 2022, 14, 12758−12765 Read Online

ACCESS | Metrics & More | Article Recommendations | Supporting Information

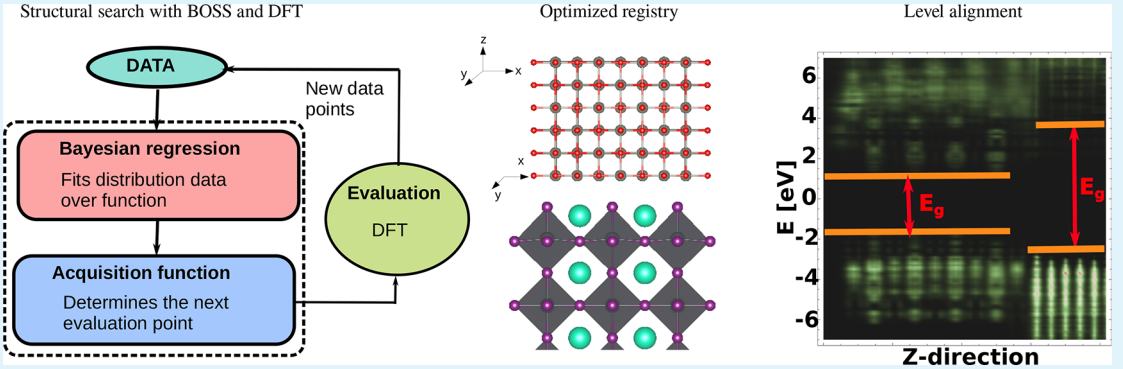

ABSTRACT: The protection of halide perovskites is important for the performance and stability of emergent perovskite-based optoelectronic technologies. In this work, we investigate the potential inorganic protective coating materials ZnO, $SrZrO_3$, and ZrO_2 for the $CsPbI_3$ perovskite. The optimal interface registries are identified with Bayesian optimization. We then use semilocal density functional theory (DFT) to determine the atomic structure at the interfaces of each coating material with the clean CsI-terminated surface and three reconstructed surface models with added PbI_2 and CsI complexes. For the final structures, we explore the level alignment at the interface with hybrid DFT calculations. Our analysis of the level alignment at the coating−substrate interfaces reveals no detrimental mid-gap states but rather substrate-dependent valence and conduction band offsets. While ZnO and $SrZrO_3$ act as insulators on $CsPbI_3$, ZrO_2 might be suitable as an electron transport layer with the right interface engineering.

KEYWORDS: *interface, surface, level alignment, perovskite, transport layer, coating, density functional theory, Bayesian optimization*

1. INTRODUCTION

Halide perovskites (HPs) have emerged as promising materials for next-generation optoelectronics, as evidenced by the steep rise in power conversion efficiency of perovskite solar cells (PSCs) from 10%[1,2] to 25.5%[3] within one decade. Other viable HP applications are light-emitting diodes, lasers, and photodetectors.[4−7] HPs and HP-based devices are particularly attractive due to their ease of fabrication, low processing temperature, cost effectiveness, and availability of raw materials.[8−10] Despite HPs' exceptional optoelectronic properties, their large-scale production and commercialization is still impeded by several factors: the commonly used hybrid (organic−inorganic) HPs are known to suffer from rapid degradation on exposure to moisture, heat, or oxygen.[11−16] In addition, organic charge-transport-layer materials will generally limit the device performance due to their structural and chemical disorder.[17] For example, *Spiro*-OMeTAD, which is the most common hole-transport-layer (HTL) material in PSCs,[1,2,18−20] suffers from instability, low hole mobility and conductivity,[21] and undesirable effect on PSC stability.[22] Surface passivation with more stable materials,[23−25] especially inorganic materials, is thus important to mitigate the negative effects of ambient conditions on HP materials and devices.

These challenges could be addressed with an all-inorganic strategy.[26−28] In this strategy, inorganic materials are chosen for all device layers: (mostly Cs-based) perovskites for the photoabsorbing or emitting layer, inorganic semiconductors as electron- and hole-transport layers, and inorganic insulators as charge-blocking materials. In this context, protective inorganic coatings have been proposed.[29−32] It would be particularly beneficial if the coating materials could also serve as electron-transport (ETL) or hole-transport layers (HTL). So far, the studied inorganic interlayer materials in perovskite-based optoelectronic devices are mainly common binary compounds. Typical examples include TiO_2,[33−35] SnO_2,[36−39] and ZnO[34,39]

Received: November 15, 2021
Accepted: February 18, 2022
Published: March 4, 2022

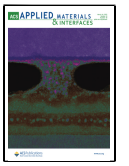

for ETLs, CuI,[40,41] NiO,[42−45] graphene oxide,[46] and CuSCN[45] for HTLs, and alkali-metal halides for charge-blocking layers.[47−50]

In our previous work, we applied a data-driven approach to discover inorganic materials suitable for perovskite-based devices with the aim of further enhancing the device performance and stability.[32] We developed a three-stage scheme as shown in Figure 1. At stage 1, we screened a

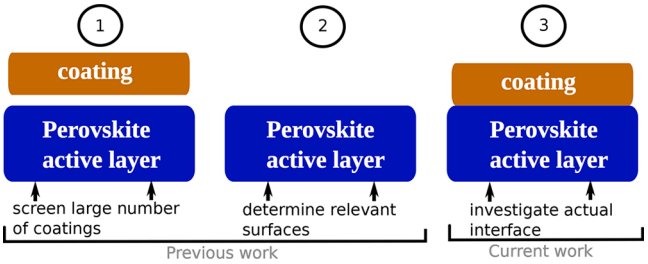

Figure 1. Conceptual workflow of identifying and characterizing suitable perovskite coating materials.

materials database for inorganic coating materials that meet a series of requirements such as band gap, stability, transport properties, and crystal structure.[32] Stage 2 identifies the stable surface structures of $CsPbI_3$ and $CH_3NH_3PbI_3$ under different growth conditions, for which we carried out a surface-phase-diagram analysis based on density-functional-theory (DFT) and *ab initio* thermodynamics.[51,52]

This work presents stage 3, which computationally estimates whether the materials that pass the screening at stage 1[32] are indeed good coating candidates for HPs. To this end, we investigate the interfaces between the candidate coatings and a series of HP surface models produced at stage 2[51] using DFT. The surface registry match between the perovskite and the coating was determined by Bayesian optimization (BO) active learning, based on the minima in the binding energy landscape. The minima of the energy landscape corresponds to the binding energy (E_b) of the most stable registry. We chose α-$CsPbI_3$ as the prototype HP model system for this first case study, while similar systems such as γ-$CsPbI_3$ and $CH_3NH_3PbI_3$ will be the subject of future work.

The remainder of this paper is organized as follows. We present a brief description of our computational approach in Section 2. In Section 3, we present the results from the BOSS/DFT calculations, analyze the features of the optimized interface structures, and establish the level alignments at the coating−perovskite interface for all coatings and substrates. Section 4 presents a brief discussion of our results. We conclude with a summary of our findings in Section 5. Computational details are presented in Section 6.

2. COMPUTATIONAL APPROACH

We designed a three-step protocol for our interface study, as sketched in Figure 2. Step I employs the recently developed

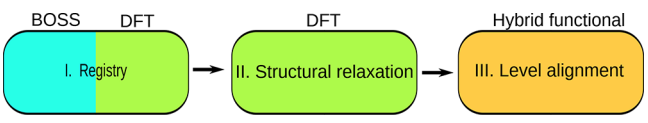

Figure 2. Protocol for computational characterization of coating−perovskite interfaces with BOSS and DFT.

Bayesian Optimisation Structure Search (BOSS) package[53] to determine the registry between the coating and the HP substrate. With this registry as the starting point, the atomic positions of the coating−perovskite interface are relaxed with DFT in step II. In step III, interfacial electronic structure calculations are carried out for the relaxed interfaces using hybrid functional DFT.

We propose such a two-step (steps I and II) structure-search strategy on the basis of the following considerations. The most stable interface geometry corresponds to the global minimum of the total-energy landscape of the coating−perovskite combination, which is a multidimensional function of a series of parameters that define the relative geometry between these two components. This total-energy landscape is very complex due to the polyatomic nature of both the coating and HP surfaces. Therefore, it is not easy to identify the most stable structure with a simple DFT structure relaxation, as different initial structures might fall to different local minima and miss the global minimum.

BOSS has already shown its power in problems such as a conformer search for organic molecules,[53,54] organic molecule adsorption at semiconductor surfaces,[53] and film growth of organic adsorbates on metallic surfaces.[55−57] In this work, we employ BOSS to tackle the interface problem between two inorganic materials (coating and HP) in step I, which we believe can efficiently narrow down the search space for further geometry relaxation in step II. In our BOSS search, state-of-the-art single-point DFT calculations are performed for different structures, and BOSS correlates the structures with an energy landscape through active learning with a BO algorithm. A surrogate model is fitted to the DFT data points employing Gaussian process regression (GPR), which is refined by acquiring further data with a smart sampling strategy. In such a way, a relatively modest number of DFT data points suffice to converge the multidimensional binding energy landscape.

For a semi-infinite slab with a thin coating layer, the band gap deep in the bulk is the same for any surface reconstruction or defect. For this reason and to provide a consistent ranking of level alignments among coatings, we use the bulk as a "model substrate" for all the interfaces. For each interface, we extracted the valence (VB) and conduction band (CB) offsets from the spatially resolved local density of states (LDOS) of Figure S5 in the Supporting Information. The offsets are then added (or subtracted) from the bulk conduction band minimum (CBM) (or valence band maximum, VBM) to create the alignments here. Our bulk band structure and LDOS plots are based on a hybrid functional. We also included spin−orbit coupling (SOC) in the bulk band structure calculation. On the basis of our previous works, we expect the inclusion of SOC to shift the CBM down (into the gap), which will lead to a reduction of the band gap energy. To account for the changes resulting from SOC, we will shift the VBM and CBM of the bulk LDOS for our final coating−perovskite interface level alignments. Details of these calculations are outlined in Section 6.

3. RESULTS

In this work, we find the stable registry and interface structure, analyze the electronic properties, and establish the level alignment at the coating−perovskite interfaces. We considered $SrZrO_3$ (cubic, $Pm\bar{3}m$), ZnO (cubic, $Fm\bar{3}m$), and ZrO_2 (tetragonal $P4_2/nmc$) as coatings on the basis of results from

https://doi.org/10.1021/acsami.1c21785
ACS Appl. Mater. Interfaces 2022, 14, 12758−12765

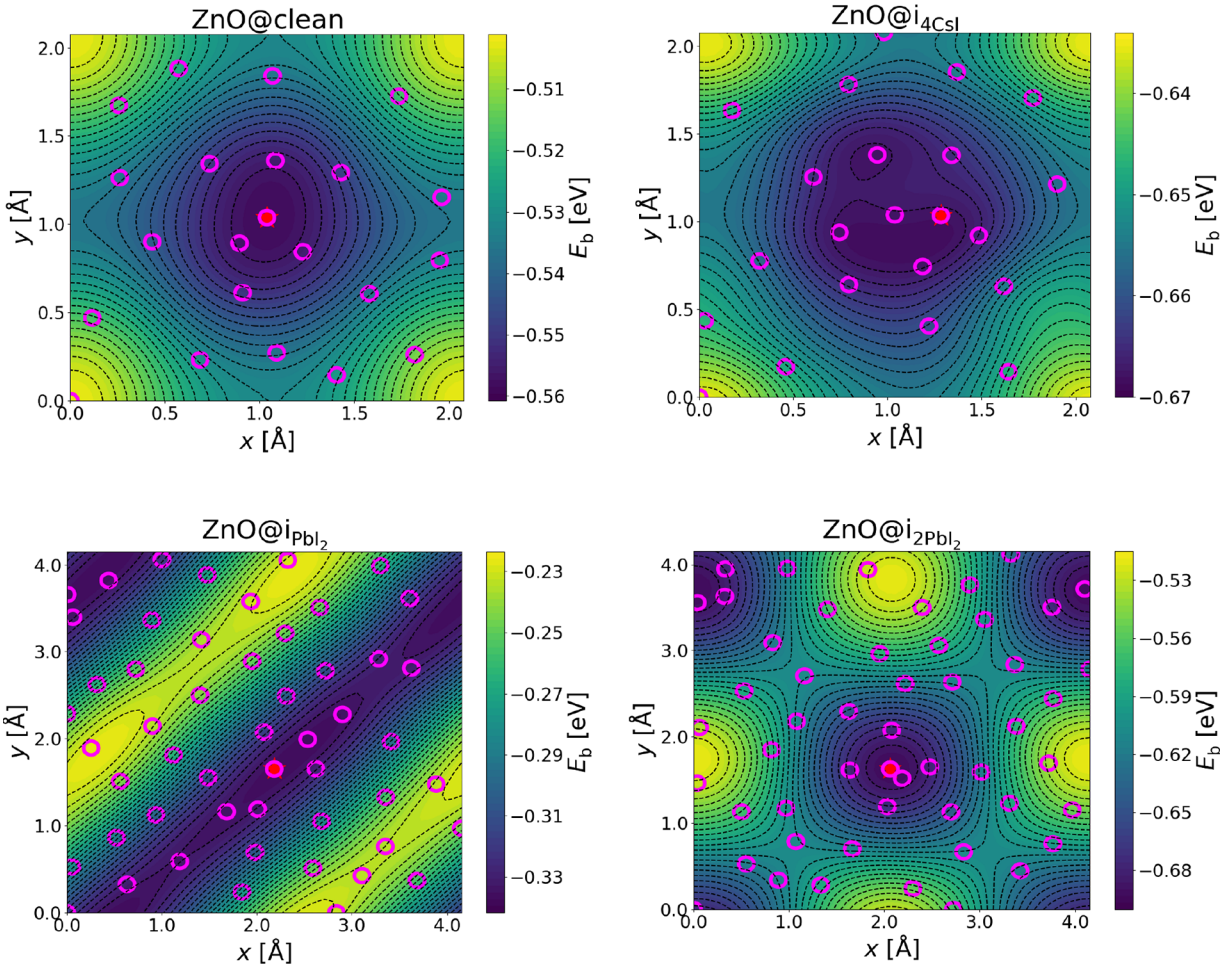

Figure 3. Binding energy landscapes of perovskite−coating with BOSS. The pink circles and red stars depict the acquisition points and minimum potential energies, respectively, as the coating is translated by x, y on the substrate.

our previous study.[32] For the substrate, we investigated both the ideal clean CsI-terminated (CsI-T) and reconstructed surface models with adatoms (of $CsPbI_3$) to simulate different synthesis conditions. The selected surface reconstructions are taken from ref S1, in which they were determined to be the most relevant reconstructions. We used the stable reconstructed surface models clean CsI-T surface, i_{PbI_2}, i_{2PbI_2}, and i_{4CsI} of $Pm\bar{3}m$ $CsPbI_3$. i_X denotes adatom structures with X = PbI_2, $2PbI_2$, 4CsI. Details of the computations are outlined in Section 6. This section will present and discuss the binding energy landscapes and optimized interface structures for ZnO on the four substrates as a prototype. We use ZnO as a prototype because, of all the coatings in this work, it is the most studied transport layer in PSCs. Similar results for the other coatings are presented in the Supporting Information. The level alignments at the coating−perovskite interface for all of the structures in this work will also be presented and discussed.

3.1. Binding Energy Landscapes from BOSS. Figure 3 shows the two-dimensional (2D) binding energy landscapes for ZnO@clean, ZnO@i_{PbI_2}, ZnO@i_{2PbI_2}, and ZnO@i_{4CsI}. The 2D binding energy landscapes for $SrZrO_3$ and ZrO_2 on the four substrates are shown in Figure S1 in the Supporting Information. The pink circles depict the acquisition points and the red stars the minimum potential energies, which corresponds to the minimum binding energy (E_b) of the surrogate models. The yellow shades in the color map depict regions of high binding energy followed by green shades, with the dark blue shades showing the lowest energies. Here, x and y are the translations of the coating in the x and y directions from some initial origin. Due to the periodicity of the system in $x - y$, these displacements describe the entire search domain.

The binding energy landscapes for ZnO@clean and ZnO@i_{4CsI} (top panels in Figure 3) exhibit an x and y range of 0.00−2.08 Å, representing the smallest unit cell of the coating@perovskite interface. For a 3 × 3 × 3 coating on a 2 × 2 substrate, the primitive unit cell of the ensemble is one-sixth of the supercell, which corresponds to a search space of 0.00−2.08 Å. In the case of ZnO@i_{PbI_2} and ZnO@i_{2PbI_2}, the interface commensurability changes due to the added PbI_2 complexes. For these, we used a search space of one-third of the supercell corresponding to 0.00−4.15 Å. The registries with the lowest binding energies are given in Table S2 in the Supporting Information.

Due to the similar search spaces for ZnO@clean and ZnO@i_{4CsI}, the binding energy landscapes are almost the same and their minimum energies (red stars) are both located at the center of the landscape. In ZnO@i_{PbI_2}, the landscape looks different due to the broken periodicity emanating from the added PbI_2 unit. Similarly, the pattern in ZnO@i_{2PbI_2} is

https://doi.org/10.1021/acsami.1c21785
ACS Appl. Mater. Interfaces 2022, 14, 12758−12765

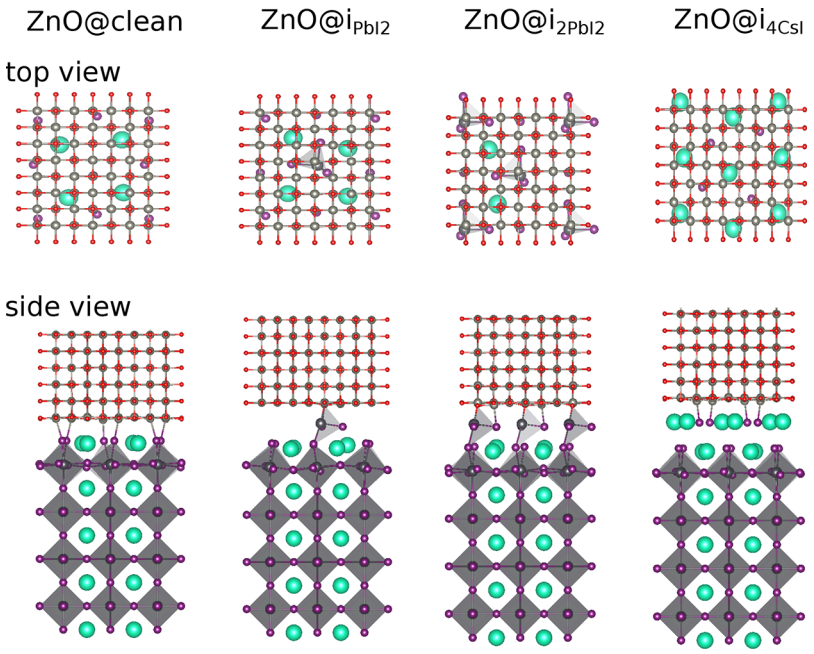

Figure 4. Optimized structure of ZnO on the clean surface and its reconstructed models: from left to right are ZnO@clean, ZnO@i$_{PbI_2}$, ZnO@i$_{2PbI_2}$, and ZnO@i$_{4CsI}$. Cs, Pb, I, Zn, and O are displayed in green, black, purple, light gray, and red, respectively. The PbI_6 octahedra are shown in dark gray.

different. Here, a diagonal periodicity is seen due to the repeated PbI_2 unit on the surface of the substrate.

3.2. Optimized Interface Structures. Figure 4 depicts the optimized interface structures obtained from DFT relaxations of the optimal registry positions for ZnO@clean, ZnO@i$_{PbI_2}$, ZnO@i$_{2PbI_2}$, and ZnO@i$_{4CsI}$. Similar results for $SrZrO_3$ and ZrO_2 are shown in Figure S2 in the Supporting Information. Detailed structural and computational information are outlined in Section 6. We observe a rearrangement of atoms in the substrates to accommodate the lattice strain between the coatings and substrates. Specifically, the Cs−I bond lengths in the topmost substrate layers change slightly to accommodate the bonding between the bottom layers of the coatings and the CsI layers. This is more pronounced in ZnO@i$_{4CsI}$, where the topmost CsI layer is pulled into the coatings. Similarly, the Pb−I bonds in the topmost polyhedra of ZnO@i$_{PbI_2}$ and ZnO@i$_{2PbI_2}$ tilt slightly at the interface. We also observe similar features for ZrO_2- and $SrZrO_3$-based interfaces (Figure S2). Despite these changes in bond lengths, our coatings show strong bonding with the substrates with no visible structural distortions.

Table 1 gives the optimized binding energies and lattice strains for all three coatings on our four most relevant reconstructed α-$CsPbI_3$ surface models. Here, $E_b = E_{ensemble} - (E_{coating} + E_{substrate})$. The absolute lattice strain increases from $SrZrO_3$ to ZrO_2, with ZnO having the largest value. Similarly, the binding is reduced with an absolute increase in lattice strains (i.e., the absolute value of the binding energy decreases). Specifically, substrates with $SrZrO_3$ coatings show the strongest binding followed by those with ZrO_2 and ZnO coatings (Table 1). This observation can be simply explained by the fact that structures with larger mismatch have a greater energetic cost due to strain, hence leading to a decrease in binding strength. Figure S3 in the Supporting Information shows a plot of binding energies as a function of lattice strain. Structurally, we also observe a minimum rearrangement in atomic positions for ZnO and ZrO_2 on all substrates. $SrZrO_3$, on the other hand, exhibits significant rearrangement, causing shifts in atomic positions (Figure S2). These observations could also contribute to the varying binding energies, as seen in Table 1.

Table 1. Binding Energies (in eV) and Lattice Strains (in Percent) of the Three Coatings on the Four Most Relevant α-$CsPbI_3$ Reconstructed Surface Models

		binding energy			
	strain	clean	i$_{PbI_2}$	i$_{2PbI_2}$	i$_{4CsI}$
$SrZrO_3$	1.0	−5.53	−5.38	−7.03	−8.16
ZrO_2	−2.2	−2.14	−3.14	−4.85	−4.23
ZnO	4.5	−1.15	−0.73	−1.32	−2.11

3.3. Level Alignment of Coating−Perovskite Interfaces. Figure 5 summarizes the level alignments for all interfaces investigated in this work. Our band structures and LDOS plots (Figure S4−S6 in the Supporting Information) exhibit no mid-gap states. Table 2 summarizes the band offsets for all interfaces. Upon the inclusion of SOC in the bulk band structure calculation, the CBM is pulled into the gap by ∼0.8 eV while the VBM shifts up by ∼0.1 eV, reducing the bulk band gap energy to 1.34 eV. To account for the effect of SOC in our coating−perovskite interface level alignments, we shifted the VBM and CBM of the bulk LDOS by 0.1 and −0.8 eV, respectively. The band structures and LDOS of all interfaces in this work are shown in Figures S4 and S5, respectively.

In all cases, we observe a type I level alignment (straddling gap). Of all three coatings, ZrO_2-based interfaces show the largest VB offsets with ZrO_2@i$_{PbI_2}$ exhibiting the largest offset. Concomitantly, the CB offsets are the smallest. Conversely, ZnO-based interfaces (except for ZnO@i$_{PbI_2}$) show larger CB

https://doi.org/10.1021/acsami.1c21785
ACS Appl. Mater. Interfaces 2022, 14, 12758−12765

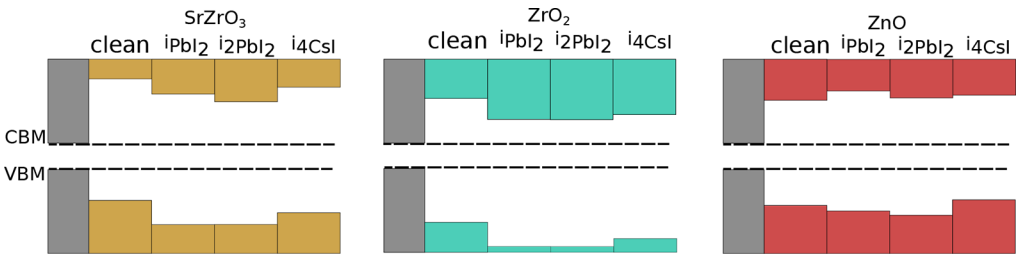

Figure 5. Band alignment at the coating−perovskite interface. The gray, red, yellow, and green shaded regions are representative of the bulk substrate, ZnO, $SrZrO_3$, and ZrO_2, respectively. The dashed lines depict the valence and conduction band edges. Here, the VBM and CBM are set to the bulk values of $CsPbI_3$ calculated with a hybrid functional including SOC.

Table 2. Valence (VB) and Conduction Band (CB) Offsets (in eV) at the Coating−Perovskite Interfaces

	band offset							
	clean		i_{PbI2}		i_{2PbI2}		i_{4CsI}	
	VB	CB	VB	CB	VB	CB	VB	CB
$SrZrO_3$	1.46	3.05	2.62	2.33	2.61	1.96	2.05	2.65
ZrO_2	2.56	2.12	3.71	1.12	3.72	1.11	3.33	1.35
ZnO	1.69	2.03	1.96	2.48	2.16	2.15	1.43	2.28

offsets. Interestingly, we observe a mixed trend in $SrZrO_3$-based interfaces. Specifically, $SrZrO_3$@clean and $SrZrO_3$@i_{4CsI} show larger CB to VB offsets while the opposite is seen in $SrZrO_3$@i_{PbI_2} and $SrZrO_3$@i_{2PbI_2}.

4. DISCUSSION

Despite a noticeable atomic displacement in the topmost layers of the substrates (Figure 4), Figure S4 and S5 in the Supporting Information show no electronic states in the band gap. The absence of such gap states is beneficial for devices, since they could act as nonradiative recombination sites. We cannot, however, exclude the presence of structural defects in real devices that introduce such gap states.

The different band alignments in Figure 5 show that the interface can be engineered to enhance charge collection or blocking. Studies have shown that ETLs (and HTLs) with a wide band gap and small CB (VB) and large VB (CB) offsets to the substrates have the potential to efficiently fulfill exciton confinement and hole-blocking (electron-blocking) functions in PSCs.[2,33] ZnO is known to be a wide-band-gap (>3 eV) n-type semiconductor that has been widely explored in optoelectronics.[34,58−60,60−62] $SrZrO_3$ is also an intrinsic perovskite semiconducting material, which means that it has the tendency to transport both electrons and holes. Conversely, ZrO_2 is a well-known insulating material that has been used as a protective coating in optoelectronics.[63,64]

Our results indicate that ZrO_2 might not only act as insulating layer on $CsPbI_3$ but could also be engineered to be an ETL. The CB offsets are the lowest we observe for all interfaces in this work, and additional iodine in the form of PbI_2 or CsI reduces the CB offsets considerably in comparison to the clean interface. This suggests that further interface modifications might lower the CB offsets sufficiently for ZrO_2 to become an ETL.

5. CONCLUSION

In summary, we have successfully studied the interactions of the coating materials ZnO, $SrZrO_3$ and ZrO_2 on four reconstructed $CsPbI_3$ surface models (clean, i_{PbI_2}, i_{2PbI_2}, and i_{4CsI}) by combining a machine-learning-based structure search method and DFT. Our optimized structures show strong bonding between the coatings and the substrates at the interfaces. Despite the changes in the atomic positions at the topmost layers of our substrates, our spatially resolved local density of states analysis exhibits no mid-gap states, which is good for transport properties across the interfaces. We further observed that both the VB and CB offsets for all coatings are large. ZrO_2 exhibits the smallest CB offset and could potentially, with the right interface engineering, serve as an ETL. Our current and previous studies serve as a starting point for future work on surface adsorbates, defects, and interface engineering of PSCs.

6. COMPUTATIONAL DETAILS

6.1. Interface Registry Search with BOSS-DFT. Data acquisitions that serve as inputs to BOSS are the binding energies (E_b) of single-point calculations at the relative perovskite−coating shift (x, y) suggested by the BOSS acquisition function. The atomic structures of the coating and perovskite are kept fixed. With each additional sampled configuration, Gaussian process models for the energetics are fitted with an uninformative prior on the mean and the model hyperparameters are optimized following the standard procedure of maximizing the log marginal likelihood. We employed the exploration-biased Lower Confidence Bound (eLCB) acquisition function, which balances exploitation against exploration.[75] The procedure is iterated until the BOSS surrogate model converges (20 iterations of the coatings on clean and i_{4CsI}, 50 for coatings on surfaces with added PbI_2 units). We monitor convergence by tracking the minima of E_b within [−3:0] eV. We then extract the global minimum from the BOSS surrogate model and use the structural model at the corresponding (x, y) coordinates as an input for DFT geometry optimization.

6.2. Interface Structural Information. We used BOSS and DFT to search for the optimal configurations of our perovskite−coating interfaces. For all of our coating materials, we used a 3 × 3 × 3 supercell, which is close to being commensurate with a 2 × 2 $CsPbI_3$ substrate. To facilitate DFT interface calculations with periodic boundary conditions, we adjusted the lattice constants of the coatings (ZnO, $a = b = c = 13.02$ Å; $SrZrO_3$, $a = b = c = 12.59$ Å; ZrO_2, $a = b = 12.19$ Å and $c = 21.57$ Å) slightly such that the three coating unit cells fit exactly onto two $CsPbI_3$ unit cells (i.e., are 12.46 Å long). In this work, we chose the cubic structure of ZnO due to its commensurabililty with the substrate even though the wurtzite

https://doi.org/10.1021/acsami.1c21785
ACS Appl. Mater. Interfaces 2022, 14, 12758−12765

structure is the most common polymorph used in optoelectronics. However, studies have shown[65−69] that, in real device engineering, the reduction in size of inorganic materials to the nanoscale induces different structural ordering relative to the most stable bulk polymorph. The perovskite surface models used as substrates in this work are the most stable reconstructed surfaces (clean, i_{PbI_2}, i_{2PbI_2} and i_{4CsI}) of α-$CsPbI_2$ from our previous work.[51]

6.3. Boundary Conditions for Structural Search. Figure 6a shows the three-step approach for the structural search with BOSS and DFT. Figure 6b depicts the registry for ZnO on the CsI-T surface model. x and y are the translations of the coating in the x−y plane away from an arbitrary initial origin ([0,0]) which corresponds to a search domain $x,y \in [0.0-2.08]$ Å for coatings on the clean and i_{4CsI} substrates. For coatings on substrates with added PbI_2 units, the search domain corresponds to $x,y \in [0.0-4.15]$ Å. By symmetry and with our choice of origin, the translations of the coating in x and y are equivalent.

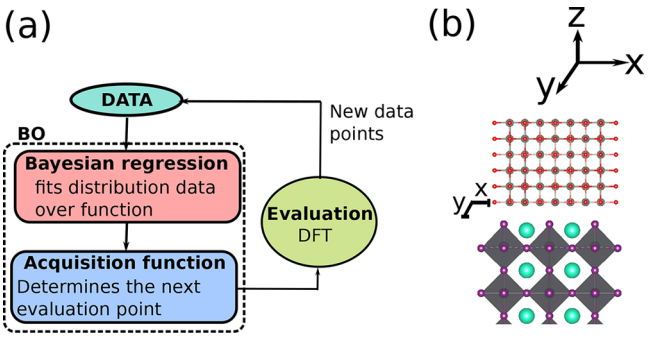

Figure 6. Workflow of the BOSS structural search and an example of its performance: (a) principles governing the buildup of a surrogate model by BOSS; (b) registry of the structure under investigation from which the binding energy is determined by varying x and y.

In all of our structural models, we kept the distance between the coating and the perovskite along the z axis constant at ∼4 Å on the basis of preliminary investigations with a three-dimensional search space. In our case, the z direction is not as important, since our tests show that it does not affect the shape or features of the 2D energy landscape and the final relaxation corrects the bonding of the atoms at the interface.

6.4. DFT and Band Alignment Computations. To overcome a numerical error from BOSS, which does not enforce symmetry, we averaged the optimal x and y translations at the local minima obtained from the BOSS/DFT run before relaxation. By fixing the bulk units (all layers below the topmost CsI and PbI_2 units) of the substrates, we then relaxed these structures, including the out-of-plane distance z, and calculated the spatially resolved local density of states (LDOS) using the hybrid Heyd−Scuseria−Ernzerhof (HSE06, simplified as HSE in this paper)[70] functional. From the HSE calculations, we deduced the band alignments at the coating−perovskite interfaces.

We used the PBEsol[71] functional with tier-1 basis sets for the single-point BOSS/DFT calculations and tier-2 basis sets for the structural relaxation (as implemented in the FHI-AIMS code[70,72]). In all cases, we used a Γ-centered 4 × 4 × 1 k-point grid. We also included dipole corrections[73] and a vacuum size of ∼40 Å to avoid dipole interactions between neighboring slabs.

In our HSE calculations, we used the standard range-separation parameter $\omega = 0.11$ bohr^{-1} but adjusted the amount of exact exchange (α) to 0.55. We also included spin−orbit coupling in our bulk band structure calculations to establish the effect of band splitting on the electronic properties. The α value was obtained by fitting our HSE +SOC band gap to the GW band gap (E_g= 1.48 eV) of the cubic (α) $CsPbI_3$ structure reported in ref 74 (see the Supporting Information for details).

■ ASSOCIATED CONTENT

Supporting Information

The Supporting Information is available free of charge at https://pubs.acs.org/doi/10.1021/acsami.1c21785.

Energy landscapes of $SrZrO_3$ and ZrO_2, binding energies of the interfaces before relaxation, optimized interface structures of $SrZrO_3$ and ZrO_2, a plot of the optimized binding energies of all interfaces as a function of lattice strain, and the band structures and spatially resolved density of states (LDOS) of all interfaces (PDF)

■ AUTHOR INFORMATION

Corresponding Author

Azimatu Fangnon − *Department of Applied Physics, Aalto University, FI-00076 Aalto, Finland;* orcid.org/0000-0002-9416-7367; Email: azimatu.fangnon@aalto.fi

Authors

Marc Dvorak − *Department of Applied Physics, Aalto University, FI-00076 Aalto, Finland;* orcid.org/0000-0001-9653-2674

Ville Havu − *Department of Applied Physics, Aalto University, FI-00076 Aalto, Finland*

Milica Todorović − *Department of Mechanical and Materials Engineering, University of Turku, FI-20014 Turku, Finland*

Jingrui Li − *Electronic Materials Research Laboratory, Key Laboratory of the Ministry of Education & International Center for Dielectric Research, School of Electronic Science and Engineering, Xi'an Jiaotong University, Xi'an 710049, People's Republic of China*

Patrick Rinke − *Department of Applied Physics, Aalto University, FI-00076 Aalto, Finland;* orcid.org/0000-0003-1898-723X

Complete contact information is available at: https://pubs.acs.org/10.1021/acsami.1c21785

Notes

The authors declare no competing financial interest.

■ ACKNOWLEDGMENTS

We acknowledge the computing resources from the CSC-IT Center for Science, the Aalto Science-IT project, and Xi'an Jiaotong University's HPC Platform. We further acknowledge funding from the Väisälä Foundation and the Academy of Finland through its Key Project Funding scheme (305632) and postdoctoral grant no. 316347. Finally, we acknowledge the AIMSS grants (316601) for their support. The data that support the findings of this study will be openly available in the Novel Materials Discovery (NOMAD) repository.[76]

■ REFERENCES

(1) Kim, H.-S.; Lee, C.-R.; Im, J.-H.; Lee, K.-B.; Moehl, T.; Marchioro, A.; Moon, S.-J.; Humphry-Baker, R.; Yum, J.-H.; Moser, J. E.; Grätzel, M.; Park, N.-G. Lead Iodide Perovskite Sensitized All-Solid-State Submicron Thin Film Mesoscopic Solar Cell with Efficiency Exceeding 9%. *Sci. Rep.* **2012**, *2*, 1.

(2) Lee, M. M.; Teuscher, J.; Miyasaka, T.; Murakami, T. N.; Snaith, H. Efficient Hybrid Solar Cells Based on Meso-Superstructured Oraganometal Halide Perovskites. *Science* **2012**, *338*, 643.

(3) Min, H.; Lee, D. Y.; Kim, J.; Kim, G.; Lee, K. S.; Kim, J.; Paik, M. J.; Kim, Y. K.; Kim, K. S.; Kim, M. G.; Shin, T. J.; Seok, S. I. Perovskite Solar Cells with Atomically Coherent Interlayers on SnO_2 Electrodes. *Nature* **2021**, *598*, 444.

(4) Chen, P.; Bai, Y.; Lyu, M.; Yun, J.-H.; Hao, M.; Wang, L. Progress and Perspective in Low-Dimensional Metal Halide Perovskites for Optoelectronic Applications. *Sol. RRL* **2018**, *2*, 1700186.
(5) Zhang, C.; Kuang, D.-B.; Wu, W.-Q. A Review of Diverse Halide Perovskite Morphologies for Efficient Optoelectronic Applications. *Small Methods* **2020**, *4*, 1900662.
(6) Dong, H.; Zhang, C.; Liu, X.; Yao, J.; Zhao, Y. S. Materials Chemistry and Engineering in Metal Halide Perovskite Lasers. *Chem. Soc. Rev.* **2020**, *49*, 951.
(7) Wang, Y.; Liu, Y.; Cao, S.; Wang, J. A Review on Solution-Processed Perovskite/Organic Hybrid Photodetectors. *J. Mater. Chem. C* **2021**, *9*, 5302.
(8) Correa-Baena, J.-P.; Saliba, M.; Buonassisi, T.; Grätzel, M.; Abate, A.; Tress, W.; Hagfeldt, A. Promises and Challenges of Perovskite Solar Cells. *Science* **2017**, *358*, 739.
(9) Rajagopal, A.; Yao, K.; Jen, A. K.-Y. Toward Perovskite Solar Cell Commercialization: A Perspective and Research Roadmap Based on Interfacial Engineering. *Adv. Mater.* **2018**, *30*, 1800455.
(10) Li, H.; Wei, Q.; Ning, Z. Toward High Efficiency Tin Perovskite Solar Cells: A Perspective. *Appl. Phys. Lett.* **2020**, *117*, No. 060502.
(11) Niu, G.; Li, W.; Meng, F.; Wang, L.; Dong, H.; Qiu, Y. Study on the Stability of $CH_3NH_3PbI_3$ Films and the Effect of Post-modification by Aluminumoxide in All-solid-state Hybrid Solar Cells. *J. Mater. Chem. A* **2014**, *2*, 705−710.
(12) Niu, G.; Guo, X.; Wang, L. Review of Recent Progress in Chemical Stability of Perovskite Solar Cells. *J. Mater. Chem. A* **2015**, *3*, 8970.
(13) Huang, J.; Tan, S.; Lund, P. D.; Zhou, H. Impact of H_2O on Organic−inorganic Hybrid Perovskite Solar Cells. *Energy Environ. Sci.* **2017**, *10*, 2284.
(14) Kim, G.-H.; Jang, H.; Yoon, Y. J.; Jeong, J.; Park, S. Y.; Walker, B.; Jeon, I.-Y.; Jo, Y.; Yoon, H.; Kim, M.; Baek, J.-B.; K, D. S.; Kim, J. Y. Fluorine Functionalized Graphene Nano Platelets for Highly Stable Inverted Perovskite Solar Cells. *Nano Lett.* **2017**, *17*, 6385.
(15) Mesquita, I.; Andrade, L.; Mendes, A. Perovskite Solar Cells: Materials, Configurations and Stability. *Renew. Sust. Energy Rev.* **2018**, *82*, 2471.
(16) Li, F.; Yuan, J.; Ling, X.; Zhang, Y.; Yang, Y.; Cheung, S. H.; Ho, C. H. Y.; Gao, X.; Ma, W. A Universal Strategy to Utilize Polymeric Semiconductors for Perovskite Solar Cells with Enhanced Efficiency and Longevity. *Adv. Funct. Mater.* **2018**, *28*, 1706377.
(17) Shao, Y.; Yuan, Y.; Huang, J. Correlation of Energy Disorder and Open-circuit Voltage in Hybrid Perovskite Solar Cells. *Nat. Energy* **2016**, *1*, 15001.
(18) Leijtens, T.; Lim, J.; Teuscher, J.; Park, T.; Snaith, H. J. Charge Density Dependent Mobility of Organic Hole-Transporters and Mesoporous TiO_2 Determined by Transient Mobility Spectroscopy: Implications to Dye-Sensitized and Organic Solar Cells. *Adv. Mater.* **2013**, *25*, 3227−3233.
(19) Im, J.-H.; Lee, C.-R.; Lee, J.-W.; Park, S.-W.; Park, N.-G. 6.5% Efficient Perovskite Quantum-Dot-Sensitized Solar Cell. *Nanoscale* **2011**, *3*, 4088.
(20) Burschka, J.; Pellet, N.; Moon, S.-J.; Humphry-Baker, R.; Gao, P.; Nazeeruddin, M. K.; Grätzel, M. Sequential Deposition as a Route to High-Performance Perovskite-Sensitized Solar Cells. *Nature* **2013**, *499*, 316.
(21) Burschka, J.; Dualeh, A.; Kessler, F.; Baranoff, E.; Cevey-Ha, N.-L.; Yi, C.; Nazeeruddin, M. K.; Gratzel, M. Tris(2-(1H-pyrazol-1-yl)pyridine)cobalt(III) as p-Type Dopant for Organic Semiconductors and Its Application in Highly Efficient Solid-State Dye-Sensitized Solar Cells. *J. Am. Chem. Soc.* **2011**, *133*, 18042−18045.
(22) Saliba, M.; Orlandi, S.; Matsui, T.; Aghazada, S.; Cavazzini, M.; Correa-Baena, J.-P.; Gao, P.; Scopelliti, R.; Mosconi, E.; Dahmen, K.-H.; Angelis, F. D.; Abate, A.; Hagfeldt, A.; Pozzi, G.; Grätzel, M.; Nazeeruddin, M. K. A Molecularly Engineered Hole-transporting Material for Efficient Perovskite Solar Cells. *Nat. Energy* **2016**, *1*, 15017.
(23) Schmidt, L. C.; Pertegá, A.; González-Carrero, S.; Malinkiewicz, O.; Agouram, S.; Espallargas, G. M.; Bolink, H. J.; Galian, R. E.; Pérez-Prieto, J. Nontemplate Synthesis of $CH_3NH_3PbBr_3$ Perovskite Nanoparticles. *J. Am. Chem. Soc.* **2014**, *136*, 850.
(24) González-Carrero, S.; Galian, R. E.; Pérez-Prieto, J. Maximizing the Emissive Properties of $CH_3NH_3PbBr_3$ Perovskite Nanoparticles. *J. Mater. Chem. A* **2015**, *3*, 9187−9193.
(25) Dong, H.; Xi, J.; Zuo, L.; Li, J.; Yang, Y.; Wang, D.; Yu, Y.; Ma, L.; Ran, C.; Gao, W.; Jiao, B.; Xu, J.; Lei, T.; Wei, F.; Yuan, F.; Zhang, L.; Shi, Y.; Hou, X.; Wu, Z. Conjugated Molecules "Bridge": Functional Ligand Toward Highly Efficient and Long-term Stable Perovskite Solar Cell. *Adv. Funct. Mater.* **2019**, *29*, 1808119.
(26) Chen, W.; Li, X.; Li, Y.; Li, Y. A Review: Crystal Growth for High-performance All-inorganic Perovskite Solar Cells. *Energy Environ. Sci.* **2020**, *13*, 1971.
(27) Liu, C.; Yang, Y.; Syzgantseva, O. A.; Ding, Y.; Syzgantseva, M. A.; Zhang, X.; Asiri, A. M.; Dai, S.; Nazeeruddin, M. K. α-$CsPbI_3$ Bilayers via One-Step Deposition for Efficient and Stable All-Inorganic Perovskite Solar Cells. *Adv. Mater.* **2020**, *32*, 2002632.
(28) Zhang, L.; Yuan, F.; Xi, J.; Jiao, B.; Dong, H.; Li, J.; Wu, Z. Suppressing Ion Migration Enables Stable Perovskite Light-Emitting Diodes with All-Inorganic Strategy. *Adv. Funct. Mater.* **2020**, *30*, 2001834.
(29) Matteocci, F.; Cinà, L.; Lamanna, E.; Cacovich, S.; Divitini, G.; Midgley, P. A.; Ducati, C.; di Carlo, A. Encapsulation for Long-term Stability Enhancement of Perovskite Solar Cells. *Nano Energy* **2016**, *30*, 162.
(30) Cheacharoen, R.; Rolston, N.; Harwood, D.; Bush, K. A.; Dauskardt, R. H.; McGehee, M. D. Design and Understanding of Encapsulated Perovskite Solar Cells to withstand Temperature Cycling. *Energy Environ. Sci.* **2018**, *11*, 144.
(31) Cheacharoen, R.; Boyd, C. C.; Burkhard, G. F.; Leijtens, T.; Raiford, J. A.; Bush, K. A.; Bent, S. F.; McGehee, M. D. Encapsulating Perovskite Solar Cells to withstand Damp Heat and Thermal Cycling. *Sustainable Energy Fuels* **2018**, *2*, 2398.
(32) Seidu, A.; Himanen, L.; Li, J.; Rinke, P. Database-driven High-throughput Study of Coating Materials for Hybrid Perovskites. *New J. Phys.* **2019**, *21*, No. 083018.
(33) Lian, J.; Lu, B.; Niu, F.; Zeng, P.; Zha, X. Electron-Transport Materials in Perovskite Solar Cells. *Small Methods* **2018**, *2*, 1800082.
(34) Tong, X.; Lin, F.; Wu, J.; Wang, Z. M. High Performance Perovskite Solar Cells. *Adv. Sci.* **2016**, *3*, 1500201.
(35) Wang, Y.; Wan, J.; Ding, J.; Hu, J.-S.; Wang, D. A Rutile TiO_2 Electron Transport Layer for the Enhancement of Charge Collection for Efficient Perovskite Solar Cells. *Angew. Chem., Int. Ed.* **2019**, *58*, 9414−9418.
(36) Anaraki, E. H.; Kermanpur, A.; Steier, L.; Domanski, K.; Matsui, T.; Tress, W.; Saliba, M.; Abate, A.; Grätzel, M.; Hagfeld, A.; Correa-Baena, J.-P. Low-Temperature Solution-Processed Tin Oxide as an Alternative Electron Transporting Layer for Efficient Perovskite Solar Cells. *Energy Environ. Sci.* **2016**, *9*, 3128.
(37) Jiang, Q.; Zhang, X.; You, J. SnO_2: A Wonderful Electron Transport Layer for Perovskite Solar Cells. *Small* **2018**, *14*, 1801154.
(38) Xiong, L.; Guo, Y.; Wen, J.; Liu, H.; Yang, G.; Qin, P.; Fang, G. Review on the Application of SnO_2 in Perovskite Solar Cells. *Adv. Funct. Mater.* **2018**, *28*, 1802757.
(39) Lin, L.; Jones, T. W.; Yang, T. C.-J.; Duffy, N. W.; Li, J.; Zhao, L.; Chi, B.; Wang, X.; Wilson, G. J. Inorganic Electron Transport Materials in Perovskite Solar Cells. *Adv. Funct. Mater.* **2021**, *31*, 2008300.
(40) Christians, J. A.; Fung, R. C. M.; Kamat, P. V. An Inorganic Hole Conductor for Organo-Lead Halide Perovskite Solar Cells. Improved Hole Conductivity with Copper Iodide. *J. Am. Chem. Soc.* **2014**, *136*, 758−764.
(41) Huangfu, M.; Shen, Y.; Zhu, G.; Xu, K.; Cao, M.; Gu, F.; Wang, L. Copper Iodide as Inorganic Hole Conductor for Perovskite Solar Cells with Different Thickness of Mesoporous Layer and Hole Transport Layer. *Appl. Surf. Sci.* **2015**, *357*, 2234−2240.

https://doi.org/10.1021/acsami.1c21785
ACS Appl. Mater. Interfaces 2022, 14, 12758−12765

(42) Kim, J. H.; Liang, P.-W.; Williams, S. T.; Cho, N.; Chueh, C.-C.; Glaz, M. S.; Ginger, D. S.; Jen, A. K.-Y. High-Performance and Environmentally Stable Planar Heterojunction Perovskite Solar Cells Based on a Solution-Processed Copper-Doped Nickel Oxide Hole-Transporting Layer. *Adv. Mater.* **2015**, *27*, 695−701.
(43) Islam, M. B.; Yanagida, M.; Shirai, Y.; Nabetani, Y.; Miyano, K. An Inorganic Hole Conductor for Organo-Lead Halide Perovskite Solar Cells. Improved Hole Conductivity with Copper Iodide. *ACS Omega* **2017**, *2*, 2291−2299.
(44) Chen, W.; Wu, Y.; Yue, Y.; Liu, J.; Zhang, W.; Yang, X.; Chen, H.; Bi, E.; Ashraful, I.; Grätzel, M.; Han, L. Efficient and Stable Large-Area Perovskite Solar Cells with Inorganic Charge Extraction Layers. *Science* **2015**, *350*, 944.
(45) Subbiah, A. S.; Halder, A.; Ghosh, S.; Mahuli, N.; Hodes, G.; Sarkar, S. K. Inorganic Hole Conducting Layers for Perovskite-Based Solar Cells. *J. Phys. Chem. Lett.* **2014**, *5*, 1748−1753.
(46) Wu, Z.; Bai, S.; Xiang, J.; Yuan, Z.; Yang, Y.; Cui, W.; Gao, X.; Liu, Z.; Jin, Y.; Sun, B. Efficient Planar Heterojunction Perovskite Solar Cells Employing Graphene Oxide as Hole Conductor. *Nanoscale* **2014**, *6*, 10505.
(47) Shi, Y.; Wu, W.; Dong, H.; Li, G.; Xi, K.; Divitini, G.; Ran, C.; Yuan, F.; Zhang, M.; Jiao, B.; Hou, X.; Wu, Z. A Strategy for Architecture Design of Crystalline Perovskite Light-Emitting Diodes with High Performance. *Adv. Mater.* **2018**, *30*, 1800251.
(48) Xu, L.; Qian, M.; Zhang, C.; Lv, W.; Jin, J.; Zhang, J.; Zheng, C.; Li, M.; Chen, R.; Huang, W. In Situ Construction of Gradient Heterojunction using Organic VO_x Precursor for Efficient and Stable Inverted Perovskite Solar Cells. *Nano Energy* **2020**, *67*, 104244.
(49) Yuan, F.; Ran, C.; Zhang, L.; Dong, H.; Jiao, B.; Hou, X.; Li, J.; Wu, Z. A Cocktail of Multiple Cations in Inorganic Halide Perovskite Toward Efficient and Highly Stable Blue Light-Emitting Diodes. *ACS Energy Lett.* **2020**, *5*, 1062.
(50) Xu, J.; Xi, J.; Dong, H.; Ahn, N.; Zhu, Z.; Chen, J.; Li, P.; Zhu, X.; Dai, J.; Hu, Z.; Jiao, B.; Hou, X.; Li, J.; Wu, Z. Impermeable inorganic "Walls" Sandwiching Perovskite Layer Toward Inverted and Indoor Photovoltaic Devices. *Nano Energy* **2021**, *88*, 106286.
(51) Seidu, A.; Dvorak, M.; Rinke, P.; Li, J. Atomic and Electronic Structure of Cesium Lead Triiodide Surfaces. *J. Chem. Phys.* **2021**, *154*, No. 074712.
(52) Seidu, A.; Dvorak, M.; Järvi, J.; Rinke, P.; Li, J. Surface Reconstruction of Tetragonal Methylammonium Lead Triiodide. *APL Mater.* **2021**, *9*, 111102.
(53) Todorović, M.; Gutmann, M. U.; Corander, J.; Rinke, P. Bayesian Inference of Atomistic Structure in Functional Materials. *npj Comput. Mater.* **2019**, *5*, 1.
(54) Fang, L.; Makkonen, E.; Todorovć, M.; Rinke, P.; Chen, X. Efficient Amino Acid Conformer Search with Bayesian Optimization. *J. Chem. Theory Comput.h* **2021**, *17*, 1955.
(55) Egger, A. T.; Hörmann, L.; Jeindl, A.; Scherbela, M.; Obersteiner, V.; Todorović, M.; Rinke, P.; Hofmann, O. T. Charge Transfer into Organic Thin Films: A Deeper Insight through Machine-Learning-Assisted Structure Search. *Adv. Sci.* **2020**, *7*, 2000992.
(56) Järvi, J.; Rinke, P.; Todorović, M. Detecting Stable Adsorbates of (1S)-camphor on Cu(111) with Bayesian Optimization. *Beilstein J. Nanotechnol.* **2020**, *11*, 1577.
(57) Järvi, J.; Alldritt, B.; Krejčí, O.; Todorović, M.; Liljeroth, P.; Rinke, P. Integrating Bayesian Inference with Scanning Probe Experiments for Robust Identification of Surface Adsorbate Configurations. *Adv. Funct. Mater.* **2021**, *31*, 2010853.
(58) Sun, Y.; Seo, J. H.; Takacs, C. J.; Seifter, J.; Heeger, A. J. Inverted Polymer Solar Cells Integrated with a Low-Temperature-Annealed Sol-Gel-Derived ZnO Film as an Electron Transport Layer. *Adv. Mater.* **2011**, *23*, 1679−1683.
(59) Ro, H. W.; Downing, J. M.; Engmann, S.; Herzing, A. A.; DeLongchamp, D. M.; Richter, L. J.; Mukherjee, S.; Ade, H.; Abdelsamie, M.; Jagadamma, L. K.; Amassian, A.; Liue, Y.; Yan, H. Morphology Changes upon Scaling a High-Efficiency, Solution-Processed Solar Cell. *Energy Environ. Sci.* **2016**, *9*, 2835−2846.
(60) Liang, Z.; Zhang, Q.; Jiang, L.; Cao, G. ZnO Cathode Buffer Layers for Inverted Polymer Solar Cells. *Energy Environ. Sci.* **2015**, *8*, 3442.
(61) Yu, W.; Huang, L.; Yang, D.; Fu, P.; Zhou, L.; Zhang, J.; Li, C. Efficiency Exceeding 10% for Inverted Polymer Solar Cells with a ZnO/Ionic Liquid Combined Cathode Interfacial Layer. *Energy Environ. Sci.* **2015**, *3*, 10660.
(62) Zheng, D.; Wang, G.; Huang, W.; Wang, B.; Ke, W.; Logsdon, J. L.; Wang, H.; Wang, Z.; Zhu, W.; Yu, J.; Wasielewski, M. R.; Kanatzidis, M. G.; Marks, T. J.; Facchett, A. Combustion Synthesized Zinc Oxide Electron-Transport Layers for Ef?cient and Stable Perovskite Solar Cells. *Adv. Funct. Mater.* **2019**, *29*, 1900265.
(63) Mejía Escobar, M. A.; Pathak, S.; Liu, J.; Snaith, H. J.; Jaramillo, F. ZrO_2/TiO_2 Electron Collection Layer for Efficient Meso-Superstructured Hybrid Perovskite Solar Cells. *ACS Appl. Mater. Interfaces* **2017**, *9*, 2342.
(64) Li, Y.; Zhao, L.; Wei, S.; Xiao, M.; Dong, B.; Wan, L.; Wang, S. Effect of ZrO_2 Film Thickness on the Photoelectric Properties of Mixed-Cation Perovskite Solar Cells. *Appl. Surf. Sci.* **2018**, *439*, 506−515.
(65) Navrotsky, A. Energetic Clues to Pathways to Biomineralization: Precursors, Clusters, and Nanoparticles. *Proc. Natl. Acad. Sci. U. S. A.* **2004**, *101*, 12096.
(66) Demiroglu, I.; Bromley, S. T. Nanofilm versus Bulk Polymorphism in Wurtzite Materials. *Phys. Rev. Lett.* **2013**, *110*, 245501.
(67) Wu, D.; Lagally, M. G.; Liu, F. Stabilizing Graphitic Thin Films of Wurtzite Materials by Epitaxial Strain. *Phys. Rev. Lett.* **2011**, *107*, 236101.
(68) Freeman, C. L.; Claeyssens, F.; Allan, N. L.; Harding, J. H. Graphitic Nanofilms as Precursors to Wurtzite Films: Theory. *Phys. Rev. Lett.* **2006**, *96*, No. 066102.
(69) Bieniek, B.; Hofmann, O. T.; Rinke, P. Influence of Hydrogen on the Structure and Stability of Ultra-Thin ZnO on Metal Substrates. *Appl. Phys. Lett.* **2015**, *106*, 131602.
(70) Heyd, J.; Scuseria, G. E.; Ernzerhof, M. Hybrid Functionals Based on a Screened Coulomb Potential. *J. Chem. Phys.* **2003**, *118*, 8207.
(71) Perdew, J. P.; Ruzsinszky, A.; Csonka, G. I.; Vydrov, O. A.; Scuseria, G. E.; Constantin, L. A.; Zhou, X.; Burke, K. Restoring the Density-Gradient Expansion for Exchange in Solids and Surfaces. *Phys. Rev. Lett.* **2008**, *100*, 136406.
(72) Levchenko, S. V.; Ren, X.; Wieferink, J.; Johanni, R.; Rinke, P.; Blum, V.; Scheffler, M. Hybrid Functionals for Large Periodic Systems in an All-electron, Numeric Atom-centered Basis Framework. *Comput. Phys. Commun.* **2015**, *192*, 60−69.
(73) Neugebauer, J.; Scheffler, M. Adsorbate-substrate and Adsorbate-adsorbate Interactions of Na and K Adlayers on Al(111). *Phys. Rev. B* **1992**, *46*, 16067.
(74) Marronnier, A.; Roma, G.; Boyer-Richard, S.; Pedesseau, L.; Jancu, J.-M.; Bonnassieux, Y.; Katan, C.; Stoumpos, C. C.; Kanatzidis, M. G.; Even, J. Anharmonicity and Disorder in the Black Phases of Cesium Lead Iodide Used for Stable Inorganic Perovskite Solar Cells. *ACS Nano* **2018**, *12*, 3477−3486.
(75) Brochu, E.; Cora, V. M.; de Freitas, N. A Tutorial on Bayesian Optimization of Expensive Cost Functions, with Application to Active User Modeling and Hierarchical Reinforcement Learning. 2010, *arXiv:1012.2599*. arxiv.org e-Print archive. https://arxiv.org/abs/1012.2599.
(76) Seidu, A.; Dvorak, D.; Havu, V.; Todorovic, M.; Li, J.; Rinke, P. Novel Materials Discovery Repository. https://dx.doi.org/10.17172/NOMAD/2022.02.21-1, 2022.